A dynamic adaptive mesh refinement and space-time spectral element method for improved capturing of vortical structures in a realistic Cryogenic Fuel tank

Yang Liu[†], Cody Estebe[‡], Mehdi Vahab[‡], Mark Sussman[†], Alireza Moradikazerouni[‡], Kourosh Shoele[‡], Wei Guo*

Thermal and Fluids Analysis Workshop
TFAWS2022
September, 2022
Virtual Conference

research supported through NASA Early Stage Innovations Program

† Department of Mathematics, Florida State University

Motivation

"Efficient and reliable cryogenic fluid management (CFM) of propellant and life support storage tanks is in the critical path of nearly all future NASA human exploration missions. One of the main challenges to long-duration storage of cryogens are heat leaks through the insulation and various conduction paths that cause tank self-pressurization (Salzman, 1996). Thrusters have traditionally been used during short duration missions to settle the propellant and relieve the tank pressure rise by venting. Unfortunately, in long duration missions, the added propellant and hardware weight to accommodate the increased number of venting cycles will be quite prohibitive. Thus NASA has targeted space cryogenic storage as an area with great potential for cost saving." (Kassemi, Kartuzova, Hylton, Cryogenics 89 (2018) 1-15).

Experimental Tanks

Figure 1: CPST EDU tank during fabrication at Marshall Space Flight Center. External view of tank without MLI or foam.

Figure 8: EDU tank as installed in TS 300.

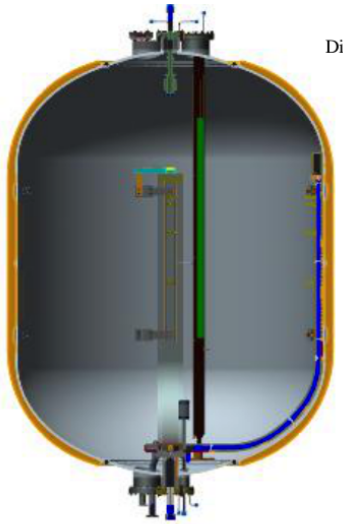

Figure 9: Cross sectional view of eCryo EDU

Figure: Cryogenic Fuel Tank for experimental purposes. Images taken from the article by Stewart (2017)

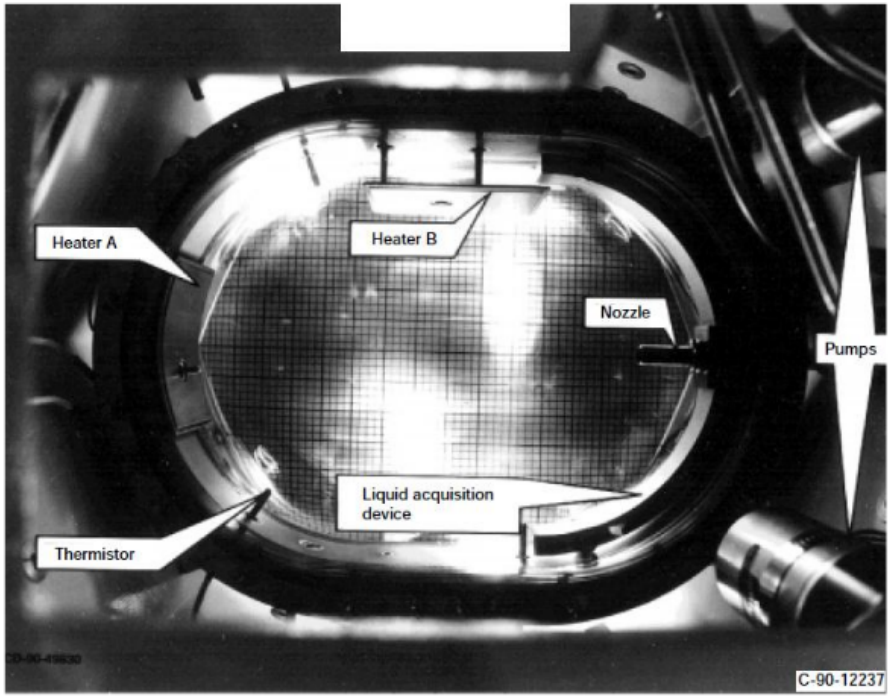

Figure 1. – TPCE experimental hardware.

Figure: Cryogenic Fuel Tank for experimental purposes. Image taken from the article by Moder and Breisacher (2015)

Motivation for Low Mach number approach

We model the liquid in the tank as an incompressible fluid. In contrast to prior work, we model the vapor as a compressible fluid with spatially uniform density and space-time varying pressure, momentum, and temperature. Our rationale for the choice of a spatially uniform vapor density is that we assume that salient features in tank flow will appear regardless of whether acoustic waves (and shock waves) are modeled in the tank. The spatially constant density assumption enables us to simulate the flow in the vapor with arbitrarily space-time high order methods (Pei et al, 2019 JSC) which are minimally dissipative. If we had modeled the vapor density as spatially varying, then slope limiting procedures must be incorporated in order to prevent the density from becoming non-positive (Harten 1987).

Remarks:

- The "PISO" algorithm ("Pressure Implicit Splitting of Operators") was used by Kartuzova and Kassemi (2016) for example. The PISO method enables one to simulate the vapor flow with a time step that exceeds the acoustic timestep constraint, but at a cost that acoustic waves are damped.
- If spatial density variations are important, e.g. in the phase change model, then it is recommended that one numerically integrate an additional spatially varying vapor density field using a positive preserving, non-conservative numerical method.
- Our method is the first space-time spectrally accurate method for simulating sharp interface, mass conserving, vapor-liquid multiphase problems.

Partial list of previous tank simulations

Reference	Model	interface treatment	jump conditions	grid	order space/ time
Panzarella and Kassemi (2003)	incomp. liquid $p_V(t)$,$T_V(t)$,$\rho_V(t)$	front tracking	body fitted	FEM	2/1
Moder and Breisacher (2015)	N/A	VOF Flow-3D	CSF	Cartesian	2/1
Kartuzova and Kassemi(2016)	Incomp. liquid comp. vapor	VOF Fluent	CSF	N/A	2/1 PISO
Stewart (2017)	Incomp. liquid comp. vapor	VOF Fluent	CSF	unstructured	2/2
Kassemi et al (2018)	Incomp. liquid comp. vapor	VOF Fluent	CSF	N/A	2/1 PISO
Sakowski et al (2019)	SINDA/FLUINT stratified liq. & vapor	Flat interface	Evap. and cond. mass transfer model	SF LUMPS	0/0
Wang et al (2019)	Incomp. liquid comp. vapor	VOF FLUENT	N/A	FVM unstructured	2/1 PISO
Zuo et al (2021)	comp. liquid, comp. vapor	VOF OpenFOAM	CSF	N/A	2/1 PIMPLE
Jiang et al(2022)	incomp. liquid, comp. vapor	VOF FLUENT	N/A	FVM unstructured	2/1 PISO
Estebe et al (2022) (this paper)	incomp. liquid comp. gas $\rho_V(t)$	MOF	GFM	Dynamic AMR	any/any

Table: Previous Numerical methods for simulating flow in cryogenic fuel tanks.

Multiphase flow with phase change; algorithms

Reference	Model (bulk)	interface treatment	jump conditions	grid	order space/ time
Panzarella and Kassemi (2003)	incomp. liquid $p_V(t)$,$T_V(t)$,$\rho_V(t)$	front tracking	body fitted	FEM	2/1
Gibou et al (2007)	incomp liquid incomp vapor	Level Set	GFM	Cartesian	2/1
Can and Prosperetti	incomp liquid $p_V(t)$,$T_V(t)$,$\rho_V(t)$	Level Set	GFM	Cartesian	2/1
Villegas et al (2016)	incomp liquid incomp vapor	Level Set	GFM	Cartesian	2/1
Stewart (2017)	Incomp liquid comp vapor	VOF Fluent	CSF	structured and unstructured, RZ	2/2
Kassemi et al (2018)	Incomp liquid comp vapor	VOF Fluent	CSF	N/A	2/1 PISO
Xia et al (2018)	"Low Mach" liquid Elastic Solid	Front Tracking	Unverdi and Tryggvason	N/A Cartesian	2/1
Palmore and Desjardins (2019)	incomp liquid incomp vapor	VOF	GFM	Cartesian	2/1
Chandra et al (2019)	comp liquid comp vapor	body fitted	body fitted	FEM Mesh Motion and Mesh Adaptation	2/2
Khalloufi et al (2020)	incomp liquid incomp vapor	Level Set	"stabilized" CSF	Dynamic Anisotropic AMR	2/1
Vahab et al (2021)	incomp liquid incomp vapor	MOF	GFM	Dynamic AMR	2/1
Wang et al (2021)	incomp liquid incomp vapor	Phase Field	GFM	Cartesian	2/1
Estebe et al (2022) (this paper)	incomp liquid comp gas $\rho_V(t)$	MOF	GFM	Dynamic AMR	any/any

Hybrid Moment of Fluid and Level Set method

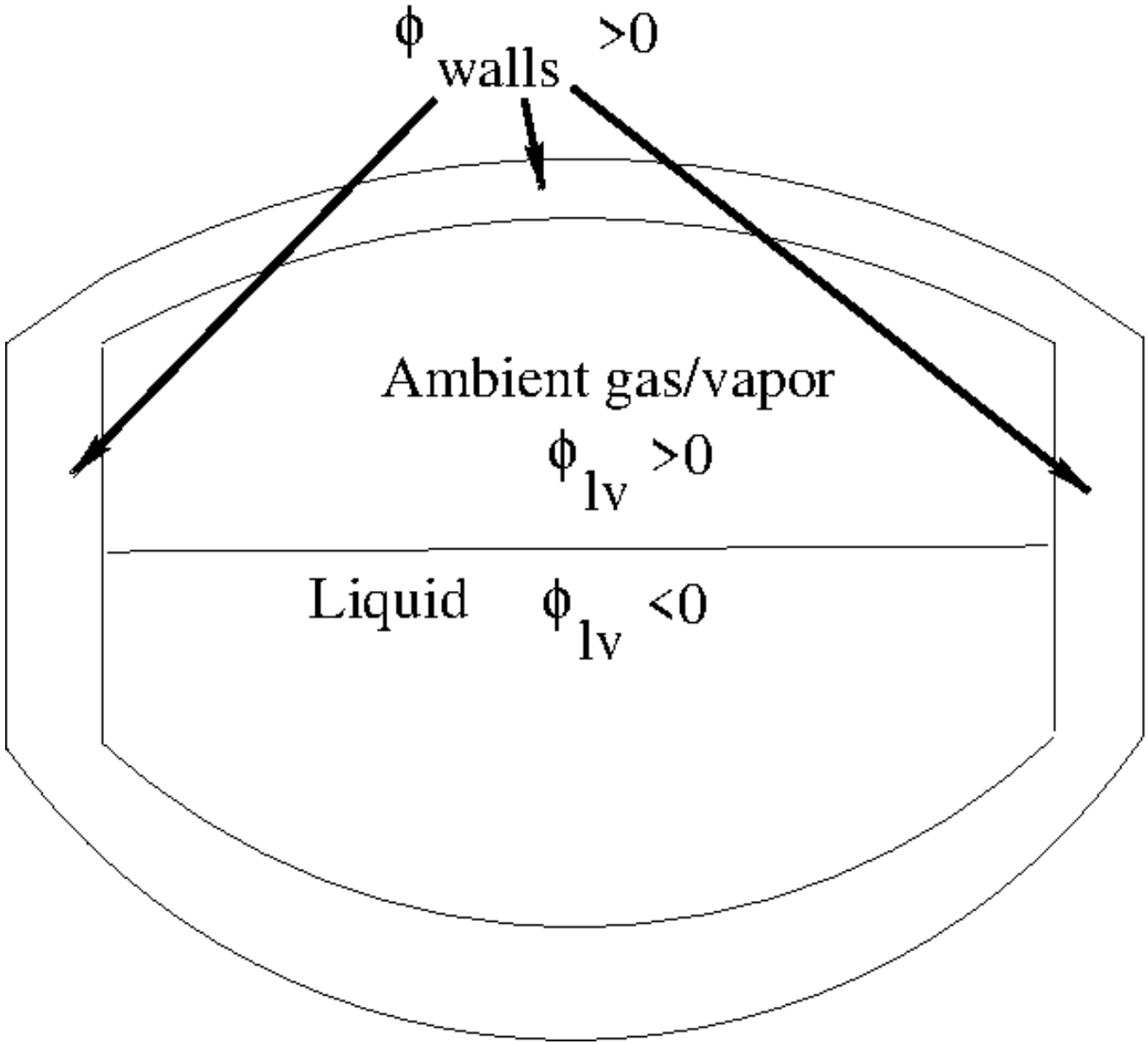

Low Mach Number $\nabla \cdot \boldsymbol{u}$ condition

$$\nabla \cdot \boldsymbol{u} = \frac{\dot{m}_{\text{source}}}{\rho_{source}} \delta(\psi_{\text{source}}) + \dot{m}(\frac{1}{\rho_v} - \frac{1}{\rho_l})\delta(\phi_{lv}) - \frac{\dot{V}_{\text{tot}} H(\phi_{lv})}{\int_\Omega H(\phi_{lv}) d\boldsymbol{x}}. \quad (1)$$

Mass Flux:

$$\dot{m} = \frac{k_l \nabla T_l \cdot \boldsymbol{n} - k_v \nabla T_v \cdot \boldsymbol{n}}{L},$$

$$\rho_l(\boldsymbol{u}_{l,t} + \boldsymbol{u}_l \cdot \nabla \boldsymbol{u}_l) = -\nabla p + \nabla \cdot (2\mu_l \mathcal{D}_l) + \rho_l(1 - \alpha_l(T_l - T_{0l}))\boldsymbol{g}, \quad (2)$$

$$(\rho_l C_{Vl} T_l)_t + \nabla \cdot (\rho_l C_{Vl} \boldsymbol{u} T_l) = \nabla \cdot k_l \nabla T_l \quad (3)$$

Ambient Gas/Vapor Momentum, Internal Energy, and or mass fraction equations

$$\rho_v(\boldsymbol{u}_{v,t} + \boldsymbol{u}_v \cdot \nabla \boldsymbol{u}_v) = -\nabla p + \nabla \cdot (2\mu_v \mathcal{D}_v) + \rho_v(1 - \alpha_v(T_v - T_{0v}))\boldsymbol{g}, \quad (4)$$

$$(\rho_v C_{Vv} T_v)_t + \nabla \cdot (\rho_v C_{Vv} \boldsymbol{u} T_v) = \nabla \cdot k_v \nabla T_v, \quad (5)$$

$$(\rho_v Y)_t + \nabla \cdot (\rho_v Y \boldsymbol{u}) = \nabla \cdot (\rho_v D \nabla Y),$$

Tank Walls Internal Energy equation

$$(\rho_{\text{walls}} C_{V,\text{walls}} T_{\text{walls}})_t = \nabla \cdot k_{\text{walls}} \nabla T_{\text{walls}} + \dot{H}_{\text{heater}} \delta(\psi_{\text{heater}}).$$

Interface Conditions

$$\phi_{lv,t} + s\frac{\nabla\phi_{lv}}{|\nabla\phi_{lv}|}\cdot\nabla\phi_{lv} = 0, \qquad \boldsymbol{u}_\Gamma = -s\boldsymbol{n},$$

$$\boldsymbol{u}_\Gamma = (\boldsymbol{u}_l\cdot\boldsymbol{n})\boldsymbol{n} + \frac{\dot{m}}{\rho_l}\boldsymbol{n} = (\boldsymbol{u}_v\cdot\boldsymbol{n})\boldsymbol{n} + \frac{\dot{m}}{\rho_v}\boldsymbol{n}.$$

$$\boldsymbol{u}_{\Gamma,l}\cdot\boldsymbol{n} - \boldsymbol{u}_{\Gamma,v}\cdot\boldsymbol{n} = \dot{m}(\frac{1}{\rho_v} - \frac{1}{\rho_l}),$$

$$p_{\Gamma,l} - p_{\Gamma,v} = \sigma\kappa_\Gamma + \boldsymbol{n}\cdot(2\mu_l\mathcal{D}_{\Gamma,l} - 2\mu_v\mathcal{D}_{\Gamma,v})\cdot\boldsymbol{n},$$

$$T_{\Gamma,l} = T_{\Gamma,v}. \tag{6}$$

$$\kappa = \nabla\cdot\frac{\nabla\phi_{lv}}{|\nabla\phi_{lv}|}.$$

$$\frac{d\rho_v}{dt} = \rho_v\frac{\dot{V}_{\text{tot}}}{\int_\Omega H(\phi_{lv})} \tag{7}$$

Evaporation Models

1. Mixture Model:

$$T_\Gamma \equiv T_{\Gamma,l} = T_{\Gamma,v} \qquad \dot{m} = \frac{k_l \nabla T_l \cdot \boldsymbol{n} - k_v \nabla T_v \cdot \boldsymbol{n}}{L},$$

$$\dot{m} = \frac{-\rho_{\text{Ambient}} D \nabla Y \cdot \boldsymbol{n}}{Y_\Gamma - 1},$$

$$X = e^{-\frac{LW_v}{R}\left(\frac{1}{T_\Gamma} - \frac{1}{T_{\text{sat}}}\right)} \qquad Y = \frac{XW_v}{XW_v + (1-X)W_{\text{Ambient}}} \qquad X = \frac{P_{\Gamma,1}}{P_{\Gamma,1} + P_{\Gamma,2}},$$

2. "No Ambient Gas" Model:

$$T_\Gamma \equiv T_{\Gamma,l} = T_{\Gamma,v} \qquad \dot{m} = \frac{k_l \nabla T_l \cdot \boldsymbol{n} - k_v \nabla T_v \cdot \boldsymbol{n}}{L},$$

$$\dot{m} = \frac{2\sigma}{2-\sigma}\sqrt{\frac{W_v}{2\pi R}}\left(\frac{P_\Gamma(T_\Gamma)}{\sqrt{T_\Gamma}} - \frac{P_{\text{eos}}(T_\Gamma)}{\sqrt{T_\Gamma}}\right),$$

$$P_\Gamma(T_\Gamma) = P_{\text{ref}} e^{-\frac{LW_v}{R}\left(\frac{1}{T_\Gamma} - \frac{1}{T_{\text{ref}}}\right)}, \qquad P_{\text{eos}}(T_\Gamma) = \rho_v (C_{P,v} - C_{V,v}) T_\Gamma.$$

references: Kassemi et al (2018), Palmore and Desjardins (2019), VILLEGAS et al (2016).

Space time slab

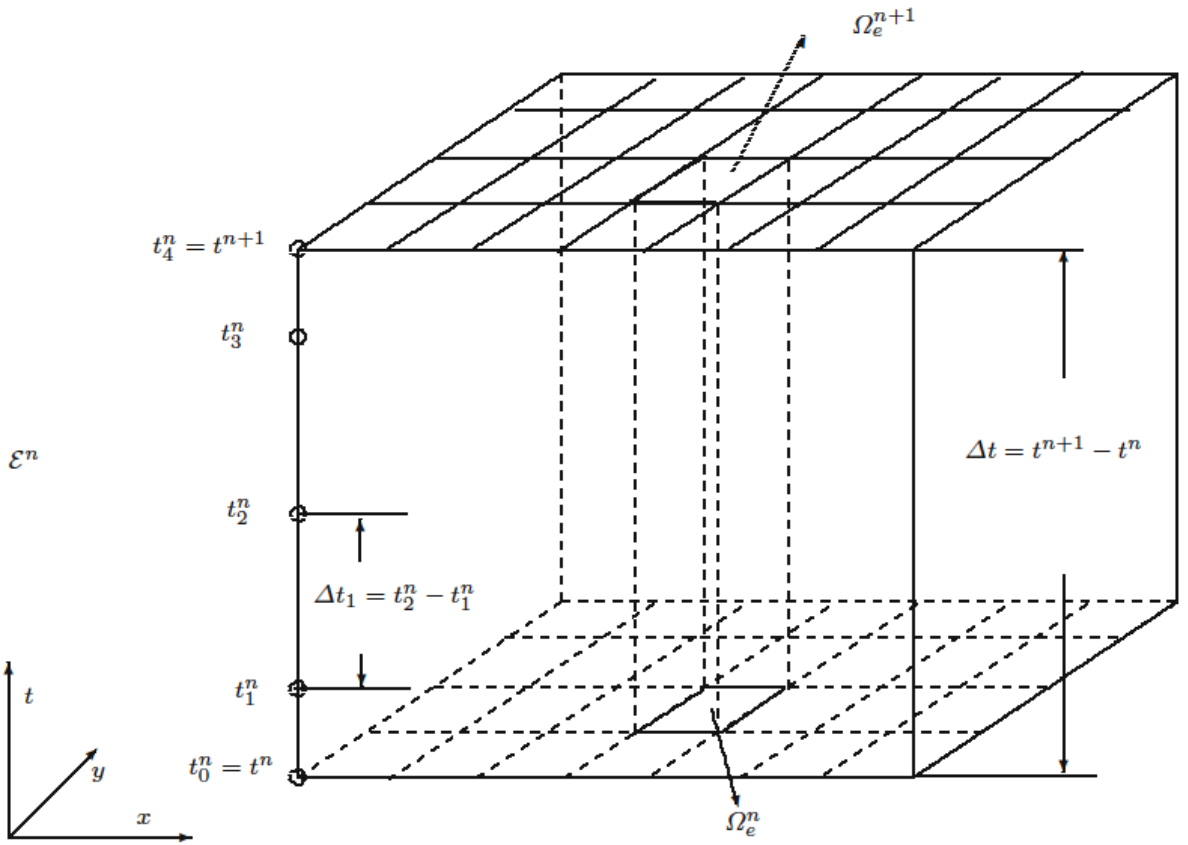

Fig. 7 An illustration of a space-time slab $\mathcal{E}^n$. The time interval $[t^n, t^{n+1}]$ is divided into 4 subintervals by choosing Legendre Gauss–Lobatto points t_m^n for $m = 0, \ldots, 4$. $\Delta t = t^{n+1} - t^n$ is referred to as a *time step size* while $\Delta t_m = t_{m+1}^n - t_m^n$ is referred to as a *time sub-step size*. The small rectangle cube is the space-time element $\mathcal{K}_e^n$ constructed by connecting Ω_e^n and Ω_e^{n+1}

Divide and Conquer versus Monolithic

$$\frac{\partial w}{\partial t} = F_1(w) + F_2(w) + \ldots F_m(w)$$

Monolithic:

$$w^{N+1} = w^N + \int_{t^N}^{t^{N+1}} \left(\sum_{j=1}^{m} F_j(w^N(\tau)) \right) d\tau_{approx}$$

Divide and Conquer:

$$w_0^{N+1} = w^N$$

For $j = 1, \ldots, m$,

$$w_j^{N+1} = w_{j-1}^{N+1} + \int_{t^N}^{t^{N+1}} F_j(w_{j-1}^{N+1}(\tau)) d\tau_{approx}$$

Spectral Deferred Correction Method

some pioneers: Minion, Layton, Bourlioux, Greengard, Rokhlin.

$$\frac{\partial w}{\partial t} = F_1(w) + F_2(w) + \ldots F_m(w)$$

For $k = 0, \ldots, P$, $j = 0$, $n = 0$, $w_j^{n,k} = w^N$
For $k = 0, \ldots, P-1$
For $n = 0, \ldots, P-1$
$j = 1$, $w_{j-1}^{n+1,k+1} = w^{n,k+1}$,
if $k = 0$ then,
For $j = 1, \ldots, m$,

$$w_j^{n+1,k+1} = w_{j-1}^{n+1,k+1} + \int_{t^n}^{t^{n+1}} F_j(w_{j-1}^{n+1,k+1}(\tau))d\tau_{low}$$

$w^{n+1,k+1} = w_m^{n+1,k+1}$

Spectral Deferred Correction Method $k > 0$

if $k > 0$ then,
For $j = 1, \ldots, m$,

$$w_j^{n+1,k+1} = w_{j-1}^{n+1,k+1} + \int_{t^n}^{t^{n+1}} F_j(w_{j-1}^{n+1,k+1}(\tau))d\tau_{low} - \int_{t^n}^{t^{n+1}} F_j(w_{j-1}^{n+1,k}(\tau))d\tau_{low} + \int_{t^n}^{t^{n+1}} F_j(w^k)d\tau_{high}$$

$w^{n+1,k+1} = w_m^{n+1,k+1}$
After the k, n, and j, loops,

$$w^{N+1} = w^{P,P}$$

The order of accuracy is P.

Tank geometry, heaters, nozzles, and liquid uisitation device (LAD)

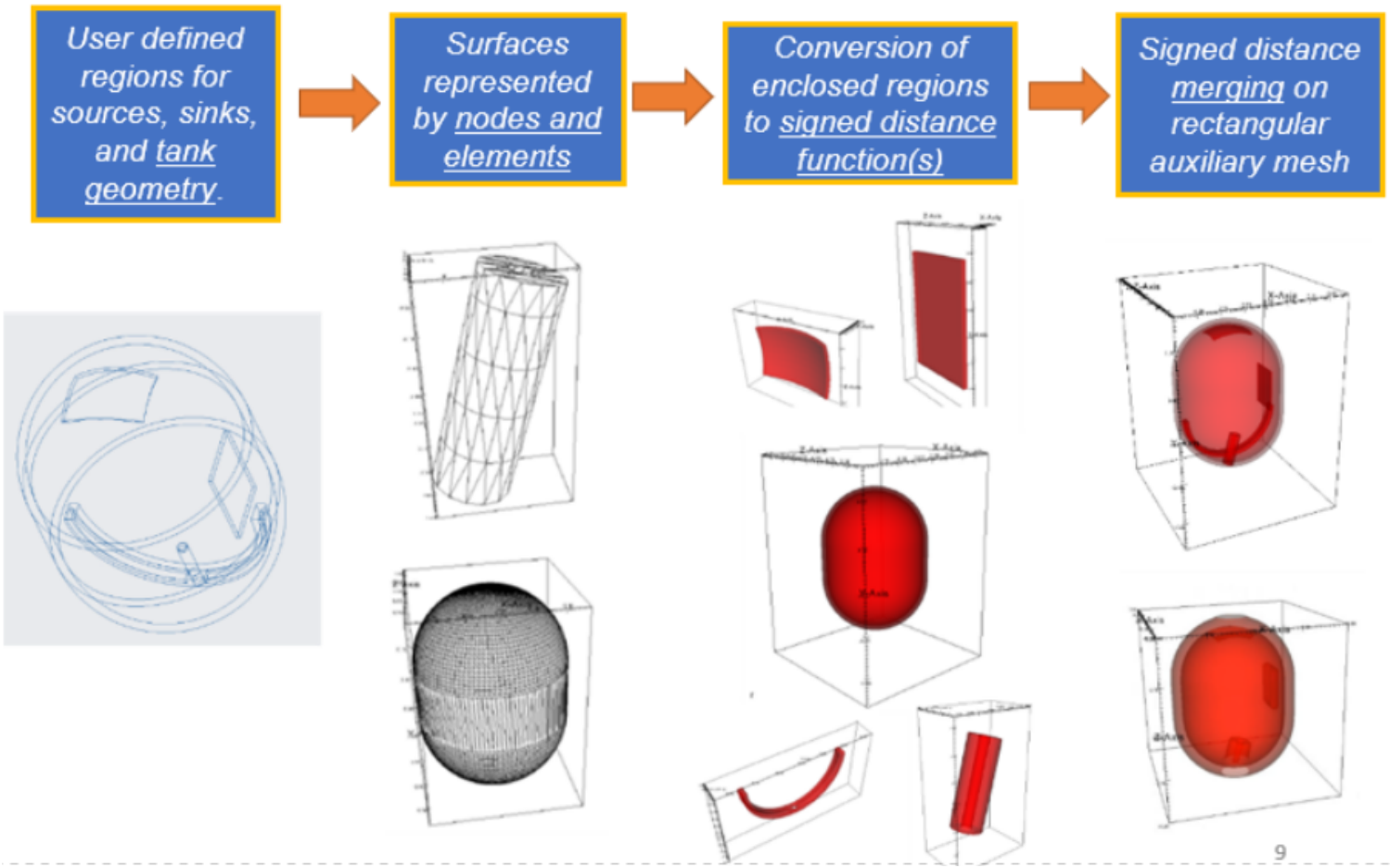

FAMU-FSU College of Engineering

CTML

TPCE full 3D Simulation with the realistic model

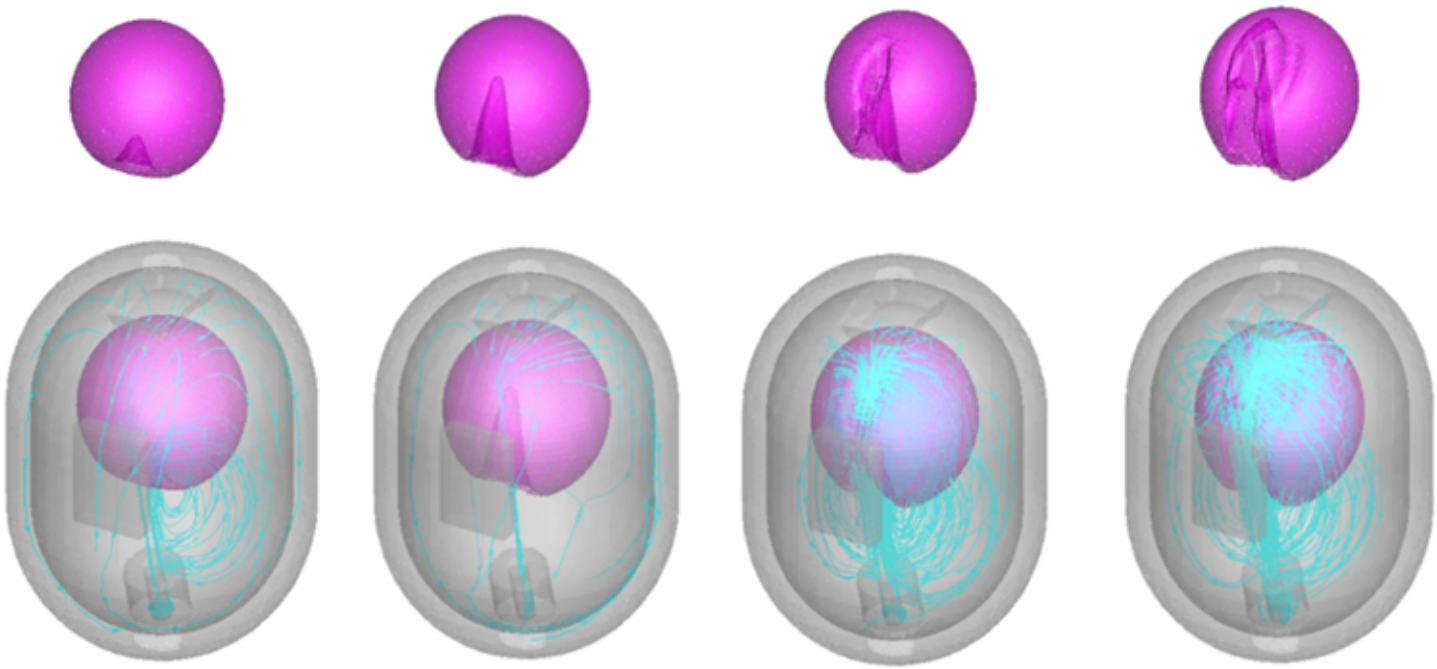

Full 3-D simulation with realistic model at different time step. Grid: 64^3 . Tilted angle of nozzle: 15 degrees.

Comparison of thin walled fine grid simulation with k walled coarse grid simulation.

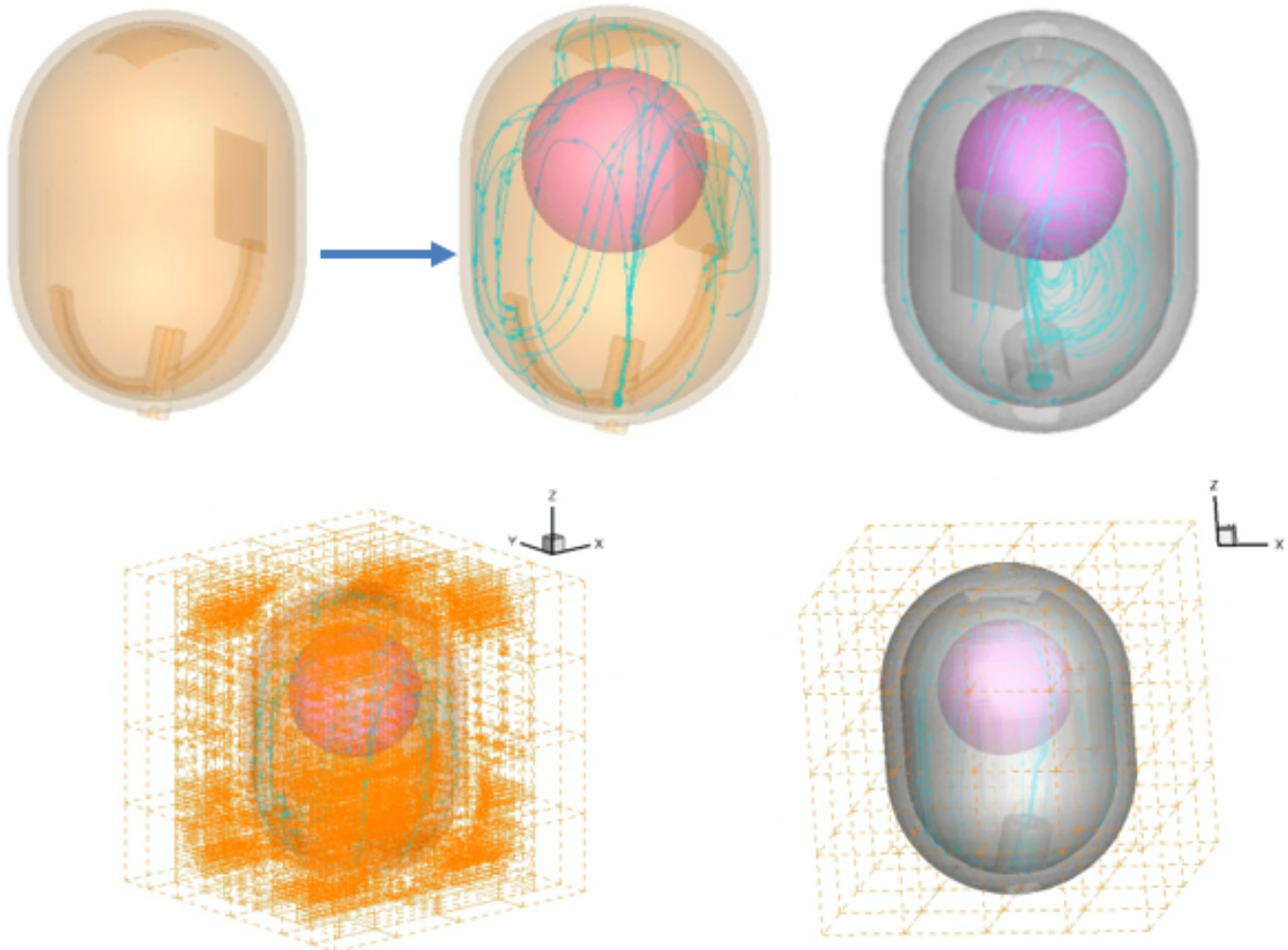

Fig. 10 Top row: Left two: thin wall model of the TPCE realistic model designing for finer resolution simulation. The simulation is on 64^3 base mesh with AMR level 1. Comparing with the previous "thick wall" model (right most figure) 64^3 base mesh with no AMR, one could observe the solid parts are

ZBOT simulation

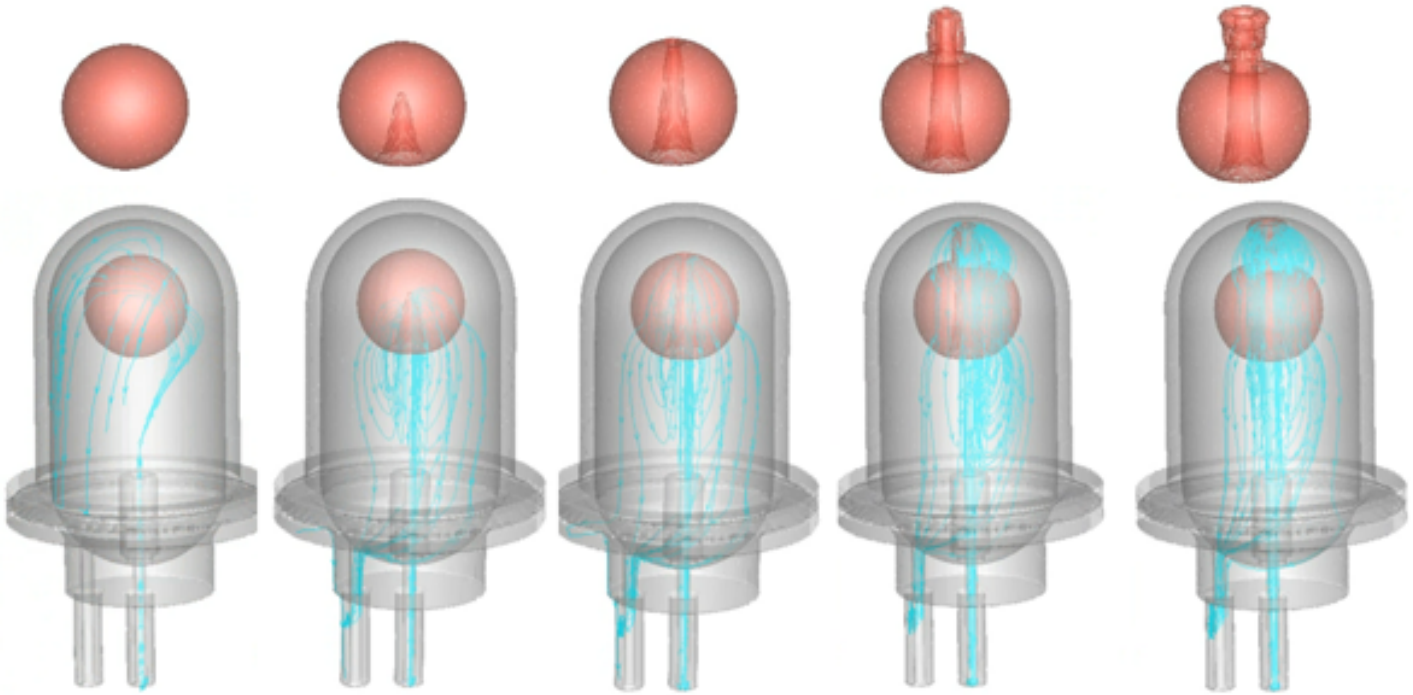

Fig 12. New ZBOT realistic model simulation, on $128 \times 128 \times 256$ uniform grid without AMR, at time 0.0018144s, 0.0105862s, 0.0123405s, 0.0158492s, 0.0176036s from left to right.

ZBOT simulation; refined grid

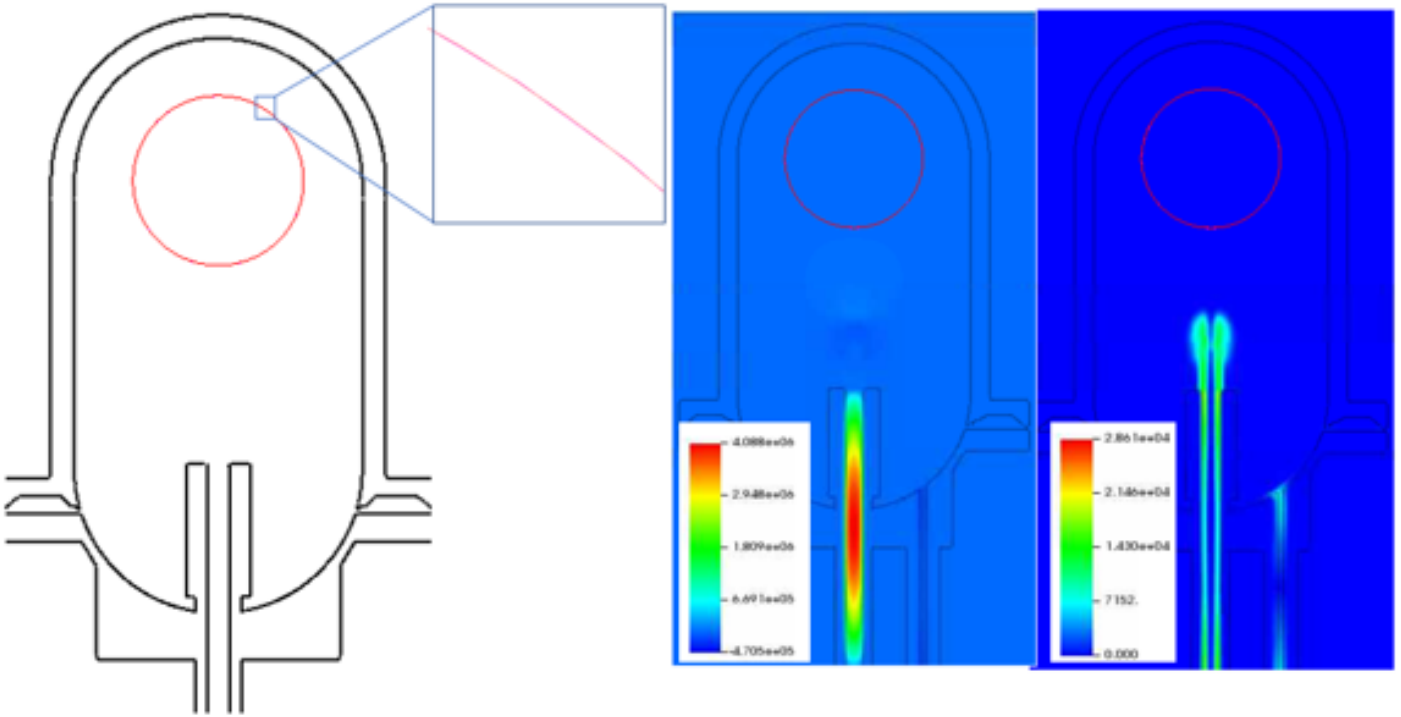

Fig 13. New ZBOT realistic model simulation, on $256 \times 256 \times 512$ uniform grid without AMR at time 0.0019497s. Left figure is an interface comparison with the previous coarser grid near the same time. Middle figure shows the pressure field. The right figure shows the vorticity.

Verification, Level 1 patch

$$0 \le x \le 1 \quad 0 \le y \le 1$$

$$\frac{D\boldsymbol{u}}{Dt} = -\nabla p + \mu \Delta \boldsymbol{u}$$

$$\frac{DT}{Dt} = \mu \Delta T$$

$$\lambda = 8\pi^2 \mu$$

$$u = -e^{-\lambda t} \sin(2\pi(x - ct)) \cos(2\pi(y - ct)) + c$$

$$v = e^{-\lambda t} \cos(2\pi(x - ct)) \sin(2\pi(y - ct)) + c$$

$$T = e^{-\lambda t} \sin(2\pi(x - ct)) \sin(2\pi(y - ct)) + \beta$$

32×32, level 0 plus level 1 patch, $\mu = 0.01$.

flow variable	second order	fourth order
T	3.0E-3	1.7E-5
$\lvert\boldsymbol{u}\rvert$	3.9E-3	4.3E-5
$\lvert\boldsymbol{\omega}\rvert$	3.3E-1	8.0E-3

Table: Sensitivity of error to the order

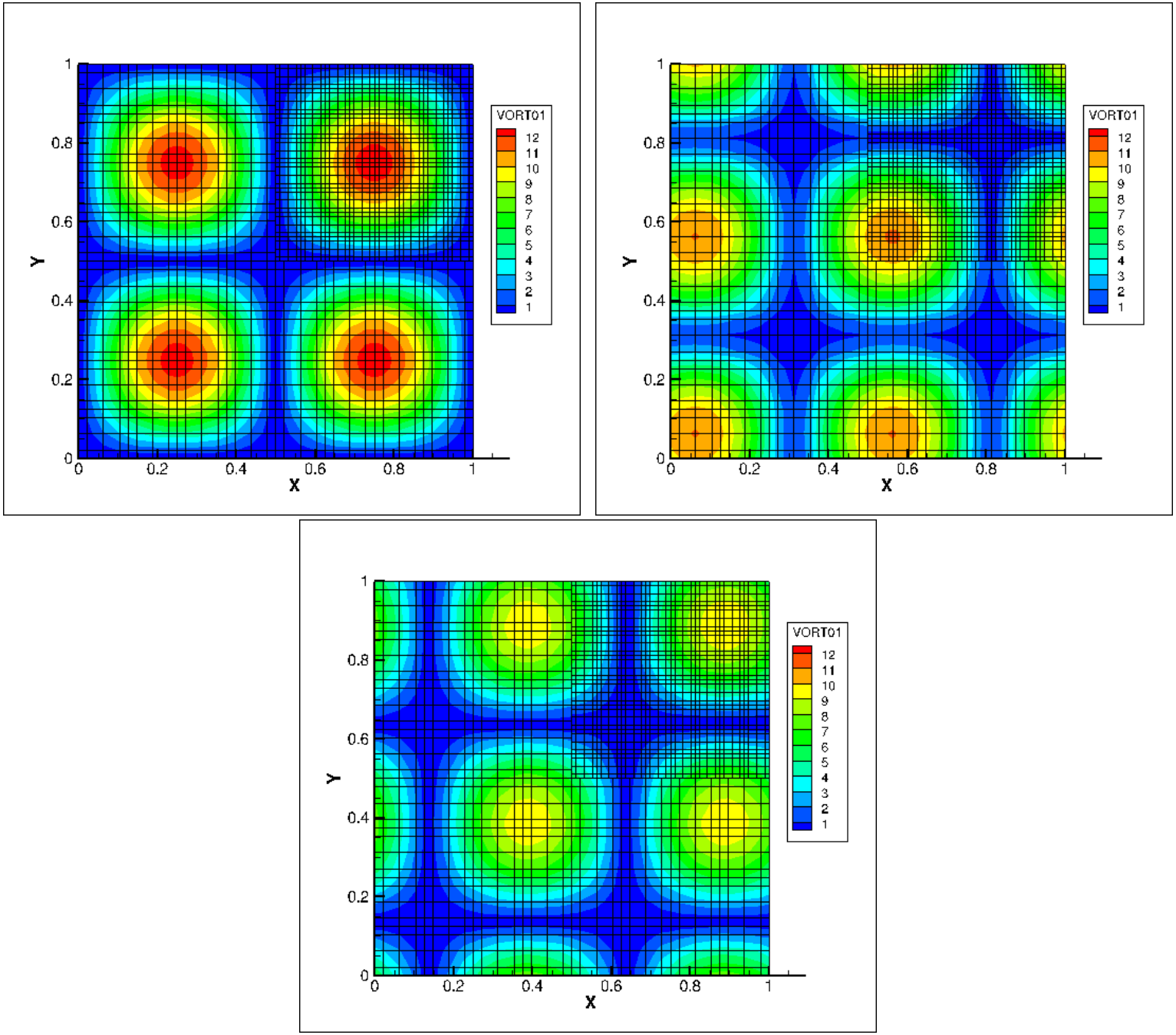

Figure: Vorticity contours for smooth verification test

periodic BC in the x direction.

$$0 \leq x \leq 1 \quad 0 \leq y \leq 2$$

$$\frac{D\boldsymbol{u}}{Dt} = -\nabla p/\rho + \mu\Delta\boldsymbol{u}\rho - \boldsymbol{y}g\beta(T - T_0)$$

$$\frac{DT}{Dt} = \mu\Delta T$$

$$u = -e^{-\lambda t}\sin(2\pi(x - ct))\cos(2\pi(y - ct)) + c$$

$$v = e^{-\lambda t}\cos(2\pi(x - ct))\sin(2\pi(y - ct)) + c$$

$$T = e^{-\lambda t}\sin(2\pi(x - ct))\sin(2\pi(y - ct)) + \beta$$

RELATIVE ERRORS, 4th order, $k = 1300$, $\mu = 1$, $c_p = 1300$, $\rho = 1400$, $\beta = 2.19E-3$, $T_0 = 293.0$, $t = 2.5$.

Δx	Δt	max. error T	max. error $\lvert\boldsymbol{u}\rvert$	max. error $\lvert\boldsymbol{\omega}\rvert$
$1/32$	$2\Delta x/3$	4.0E-1	2.3E-3	5.4E-2
$1/64$	$2\Delta x/3$	3.9E-2	1.6E-4	7.9E-3
$1/128$	$2\Delta x/3$	2.9E-3	1.1E-5	4.5E-4

Table: Sensitivity of max error to the grid size

Temperature Contours.

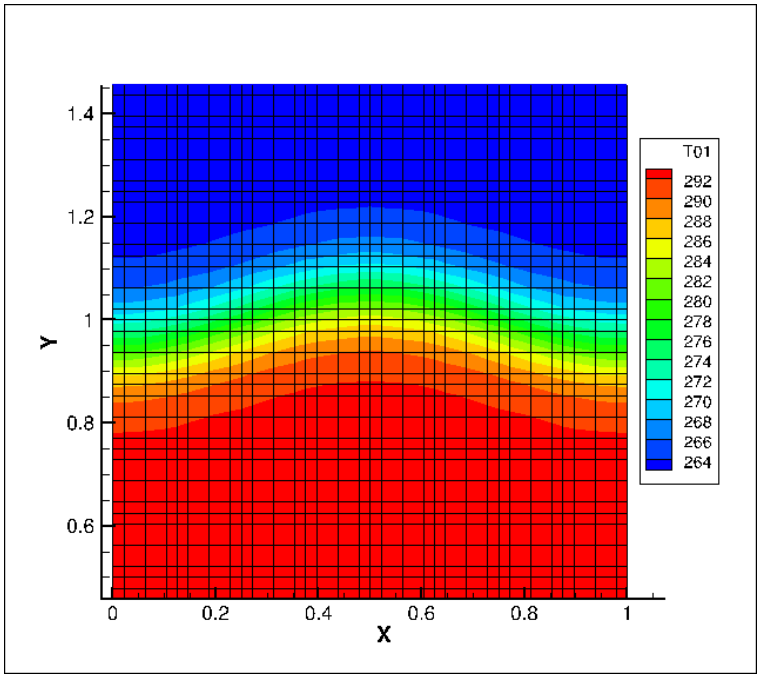

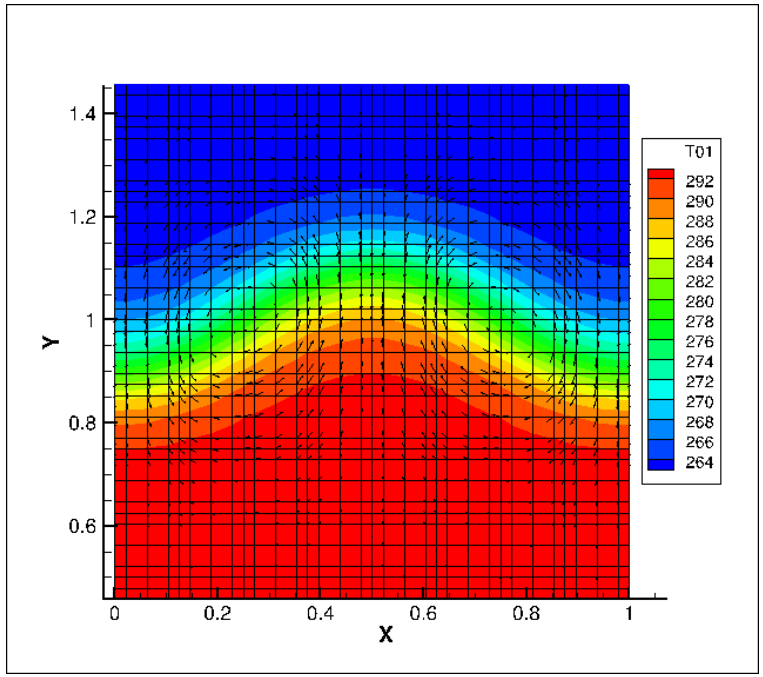

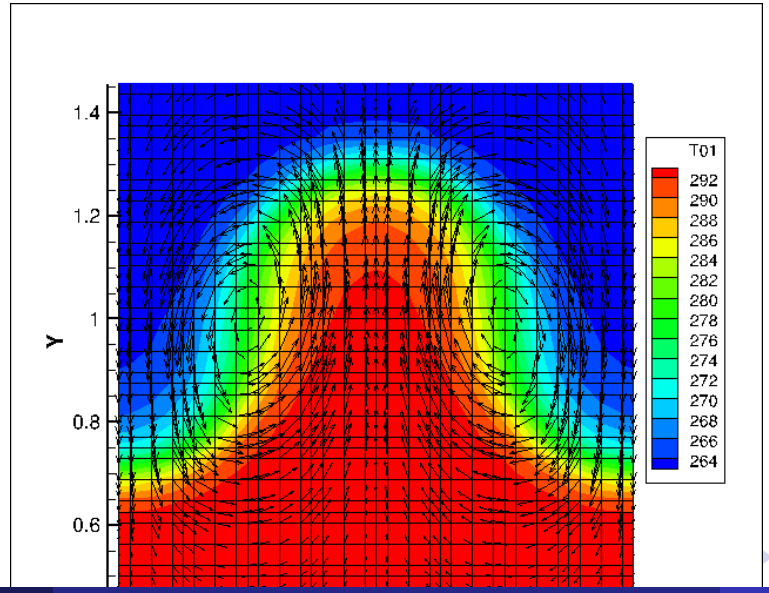

Validation: Tank Pressurization, Earth gravity.

Reference: Barsi and Kassemi (2013). Fill level: 50 percent, 2 watts, Figure 7 (blue curve).

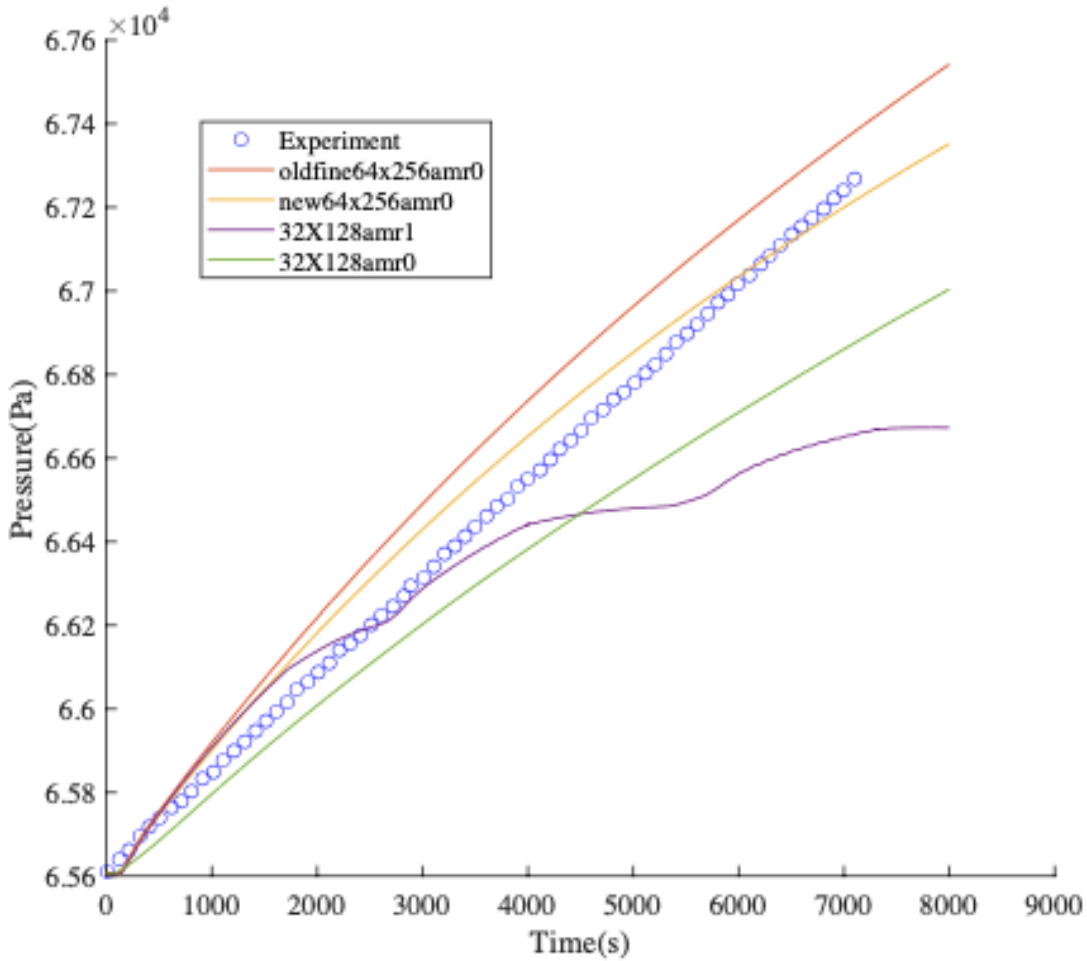

Validation: Tank Pressurization, Earth gravity.

Reference: Barsi and Kassemi (2013). Fill level: 50 percent, 2 watts, Figure 7 (blue curve). column 1: AMR grid; column 2: $t = 1250$, AMR; column 3: $t = 1250$, uniform fine; column 4: $t = 2000$, AMR; column 5: $t = 2000$, uniform fine;

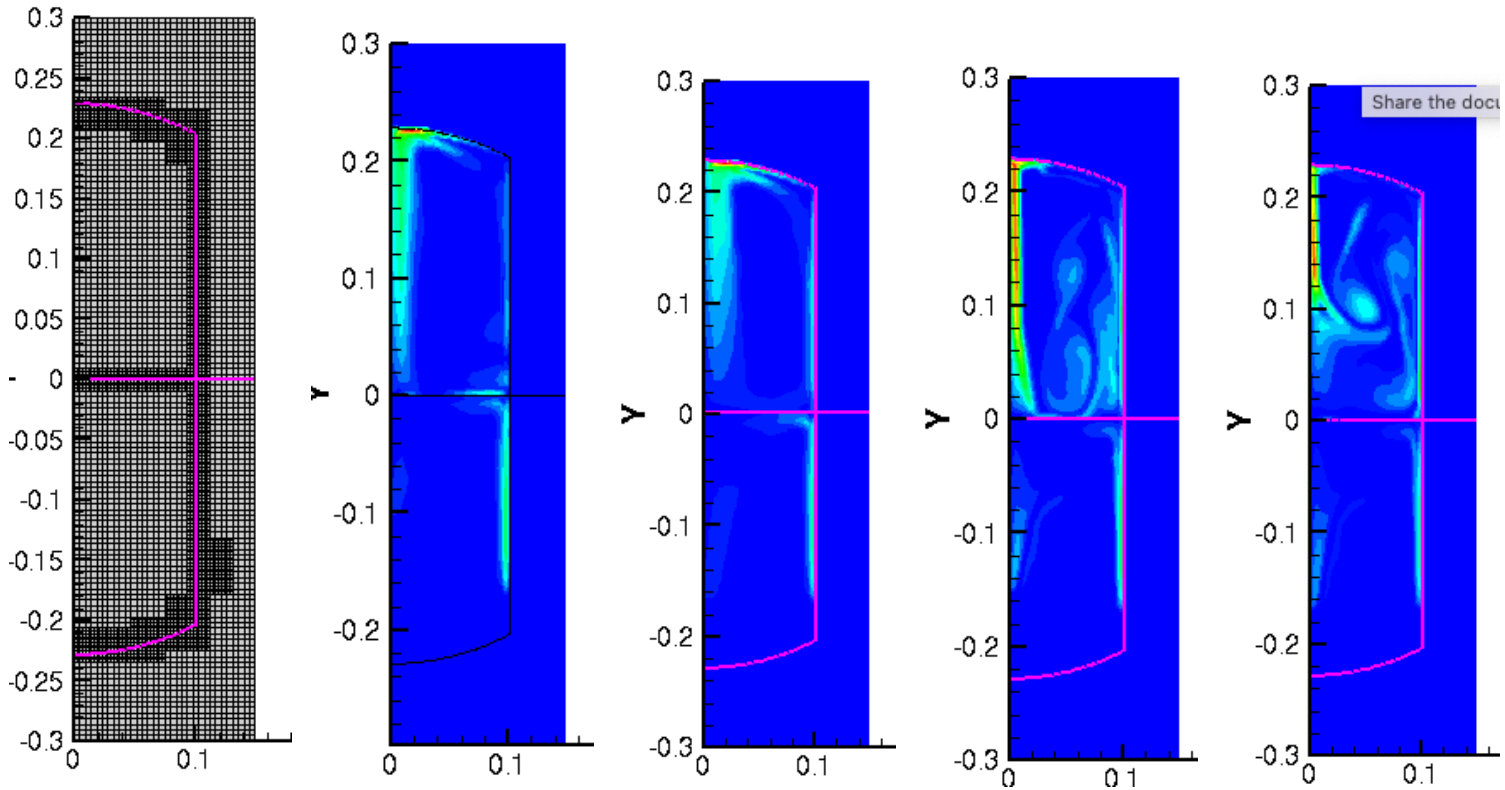

Validation: Effect of We_j on bubble ullage dynami

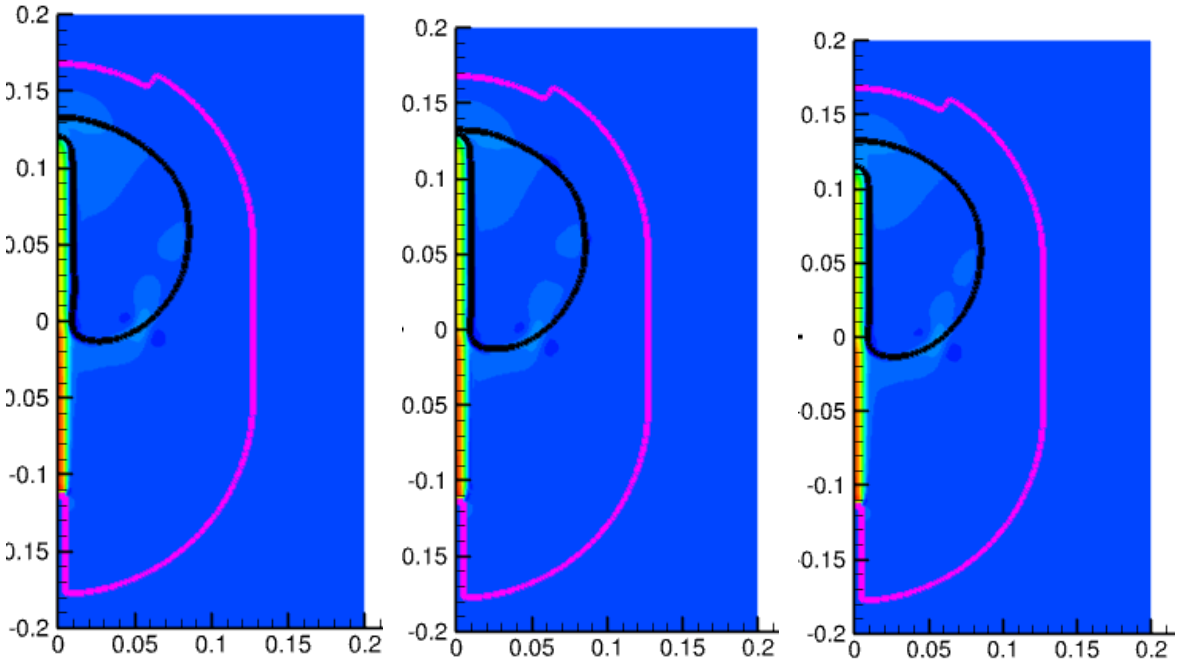

Figure: Preliminary zero-gravity 3D axisymmtric results for the simulation of bubble dynamics in the ZBOT (Kassemi, Kartuzova, and Hylton 2018) tank using the HFE7000 material, but with inflow conditions corresponding to the microgravity experiments reported by Bentz, Meserole, and Knoll (1992). The flow rate is 0.3 Litres per minute and the heater A input is 18.3 Watts. The simulation time is $t = 10.9$. $We_j = 1.97$. Left: uniform fine first order; Middle: 2nd order, AMR; Right: 1st order, AMR

Validation: Effect of We_j on bubble ullage dynami

$t = 10.94$, effective fine grid resolution 256×512.

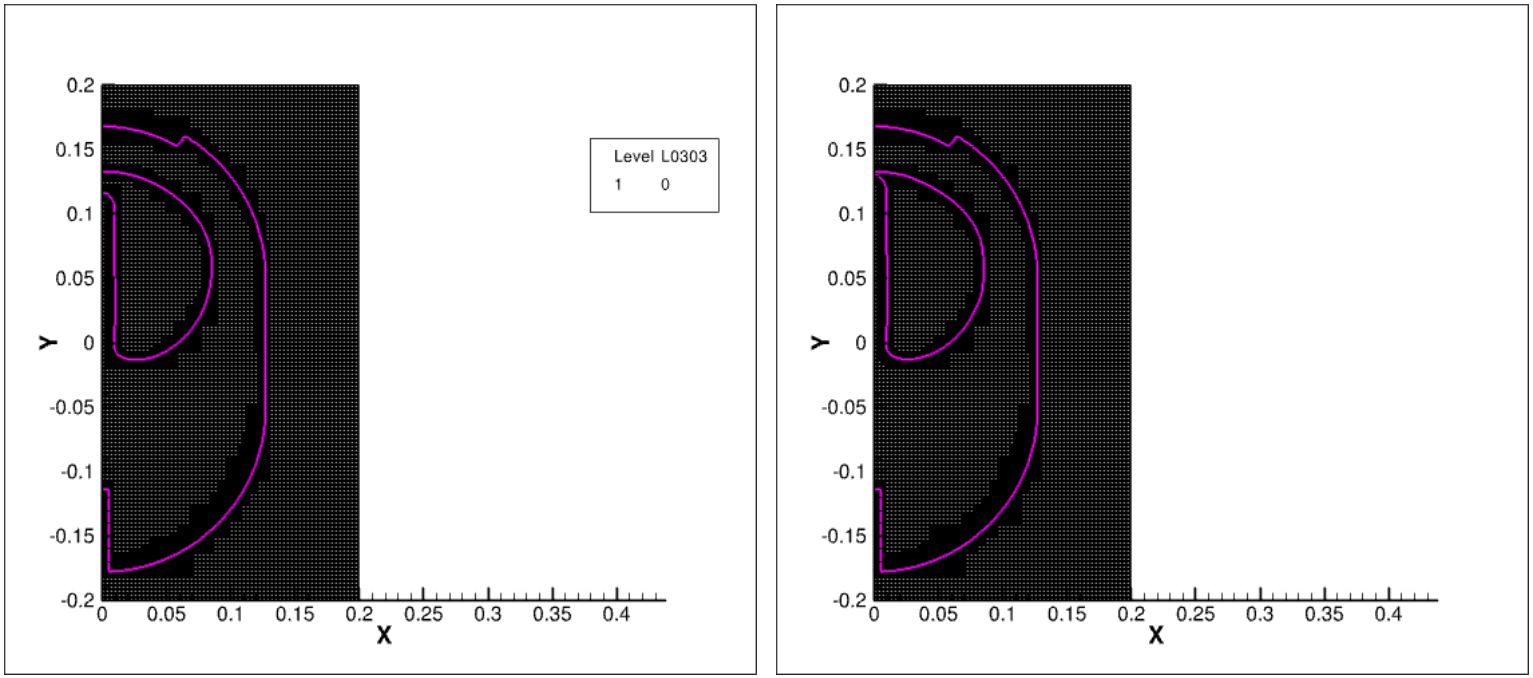

Figure: RZ TPCE test. Left: first order, Right 2nd order

Validation: Effect of We_j on bubble ullage dynami

$t = 10.94$, effective fine grid resolution 256×512.

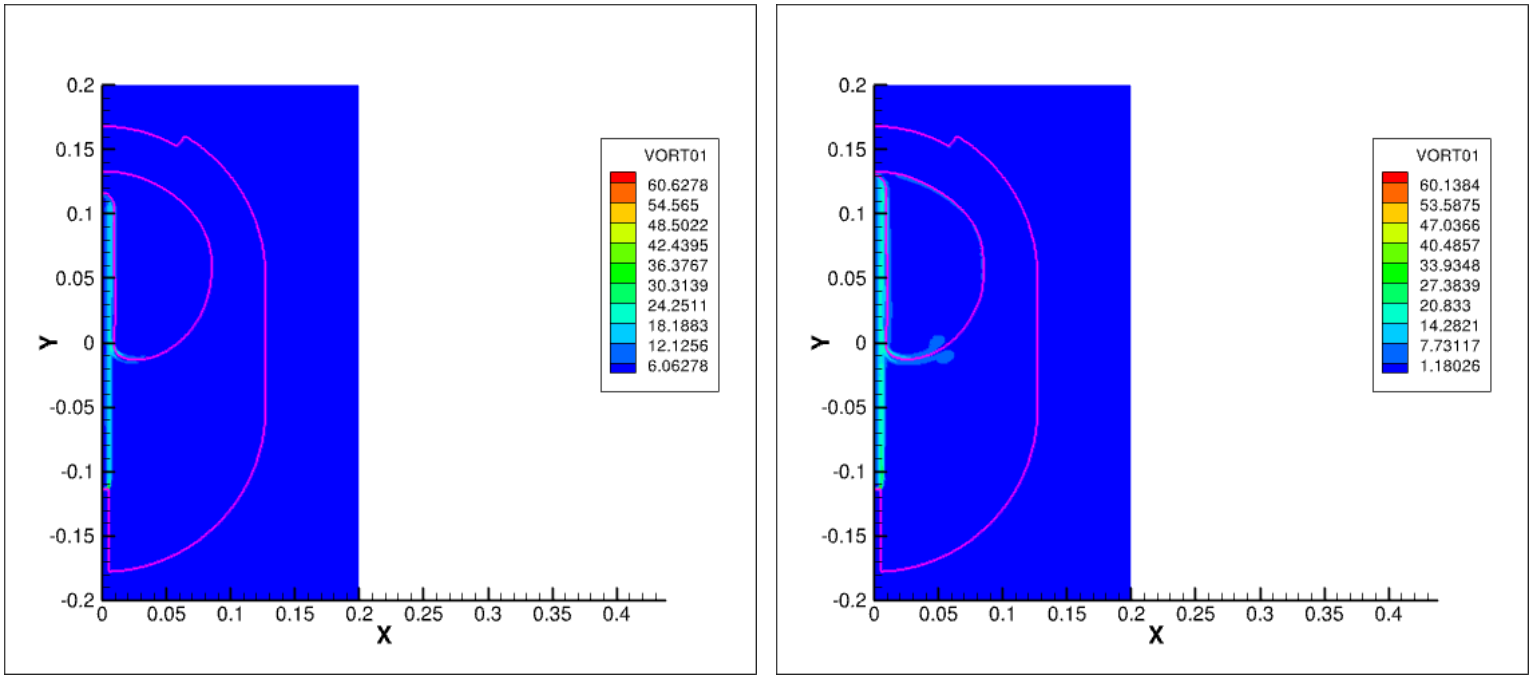

Figure: RZ TPCE test. Left: first order, Right 2nd order

Conclusions.

- Pros: space time spectral method gives "fine grid resolution" accuracy on a coarse mesh.
- Cons: overhead for space time spectral method: factor of 2 (space), factor of $P^{1/2}$ time, factor of 2 bicgstab preconditioner
- Cons: time step restriction on fine level(s) due to surface tension and convection is prohibitive. Best to avoid AMR and implement strategic "law of the wall" and/or "interface subscale" models.

research supported through NASA Early Stage Innovations Program